A bottom-up multiscale approach to model the mechanical behaviour of single osteons under multiple loading conditions

Pierfrancesco Gaziano* [a], Elisabetta Monaldo [b], Cristina Falcinelli [c], Giuseppe Vairo [a]

[a] *Department of Civil Engineering & Computer Science (DICII), University of Rome "Tor Vergata", Via del Politecnico 1, 00133 Rome, Italy*

[b] *Department of Engineering, Roma Tre University, Via Vito Volterra 62, 00146 Rome, Italy*

[c] *Department of Engineering and Geology (InGeo), G. DAnnunzio Chieti-Pescara University, Viale Pindaro 42, 65127 Pescara, Italy*

Abstract

In this paper, a novel three-dimensional finite-element based multiscale model is proposed with the aim of describing the mechanical response of single osteons. A typical osteon has been geometrically modelled as a hollow cylinder made up of coaxial subunits called lamellae. The lamellar tissue has been characterized by a refined constitutive description, based on a bottom-up multistep homogenization procedure and on modelling parameters having a clear histological meaning. The model takes into account the main bone structural features at each length scale, as well as the presence of interlamellar areas and of lacunae at osteonal level. The progressive loss of osteon structural integrity has been modelled by coupling the previous aspects with a brittle damage description, and by considering the possible occurrence of both interlaminar and intralaminar failure modes. Proposed model has been validated by numerically replicating, through home-made codes, different loading scenarios mimicking corresponding experimental test whose outcomes are available in the literature. Proposed results prove that the model is robust, accurate and therefore able to characterize the mechanical response up to failure of single osteons under different loading conditions. The model may therefore be useful for providing a more thorough understanding of how both microdamage processes and disease-/ageing-induced structural and morphological alterations of cortical bone at each length scale affect its mechanical behaviour at macroscale level.

Key words: Bone micromechanics, multiscale homogenization, anisotropic materials, damage-based finite-element modelling, osteon failure

*Corresponding Author Email address: gaziano@ing.uniroma2.it (P. Gaziano).

1 Introduction

Bone fractures, which may be caused by multiple factors, such as traumas, osteoporosis, presence of metastases or age-induced bone weakening, represent worldwide a significant public health concern, both from a human and socioeconomic viewpoint [1]. In fact, severe medical complications may often arise, including, to name a few, disabilities, cognitive and neurological alterations, cardiopulmonary affections, venous thromboembolism and possibly even the patient death [2,3]. Moreover, owing to their high trend of incidence, which is predicted to dramatically increase in the next few years, the economic burden associated to bone fractures is very consistent [1,4,5]. In this context, the main clinical objective should be the accurate prediction of bone fractures, which however at present relies on qualitative indexes lacking in specificity, such as the areal bone mineral density in the case of osteoporosis or the Mirels scoring system for metastasis-induced femoral fractures [6, 7]. The lack in specificity of the previously-mentioned indexes is essentially related to the fact that they disregard the mechanical determinants of fracture, as well as the multi-scale nature of bone material [8].

Bone is indeed a complex anisotropic material consisting of different organized hierarchical structures over multiple length scales. At the organ level, two distinct types of bone tissues characterized by different mechanical properties can be distinguished, namely the cortical (or compact) bone, dense and stiff, and the trabecular (or spongy) bone, porous and tough [9, 10]. At the microscale, cortical bone is constituted by hollow quasi-cylindrical systems running approximately parallel to the axial direction of long bones and having an average diameter of $200 \div 250$ µm, called osteons or Haversian systems [9, 11, 12]. The osteon central canal, which has a diameter averagely equal to 40 µm, is the Haversian canal. Osteons are made up of several coaxial pseudo-cylindrical layers about 3 µm in thickness wrapping around the Haversian canal, called lamellae [10, 13]. Within a single lamella, the sub-microstructural units characteristic of cortical bone, called mineralized collagen fibrils (MCFs), are arranged following a well-definite pattern [13,14]. In turn, at the nanoscale level, MCFs are constituted by Type-I collagen fibrils strengthened by crystals of a mineral phase predominantly constituted by hydroxyapatite (HA). Minor quantities of water, non-collagenous organic proteins (NCPs) and impurities are also present [11, 15–17].

All the bone constituents are combined in a remarkably effective way so as to form a properly-organized and nature-optimized material with superior mechanical properties combining high stiffness, strength and toughness [18,19]. As a consequence, accounting for bone material composition and structural organization at each length scale is fundamental to improve the understanding of bone mechanics at the macroscale level. In such a way, highly effective

novel strategies for bone fracture risk assessment can be developed on the basis of more quantitative and reliable predictions [12]. In this framework, it is well-documented that damage mechanisms at the microscale level are primarily responsible for the reduction of bone tissue resistence to fracture [20–22]. Specifically, osteons were proved to have a key role for the propagation of cracks at organ level. As such, valuable information of macroscale bone cracking processes might be better understood if the mechanical behaviour of a single osteon up to fracture is investigated [23].

Finite Element (FE) modelling represents an effective approach to investigate the micromechanics of compact bone. However, at present only few FE-based models have been developed with the aim of describing the micromechanical behaviour of osteonal bone. Hogan [24] and Crolet et al. [25] were among the first researchers to estimate the bone equivalent elastic properties through FE techniques. In particular, Hogan investigated the dependence of the elastic moduli of cortical bone on the material properties of osteon, interstitial bone, and cement lines, finding a reasonable agreement with experimental data [24]. Crolet et al. conducted a similar study but in the framework of a multiscale approach [25]. Their results, furnished however only in terms of bone homogenized elastic properties, showed good agreement with the experimental data, corroborating, in particular, the hypothesis of periodicity of collagen/HA distribution within each single osteonic lamella.

To the best of the authors' knowledge, the very first numerical model of a single osteon was developed by Prendergast and Huiskes, who aimed to investigate the relationship between damage formation, lacunar voids and local strain in the cortical bone microstructure [26]. They provided important and useful evidence that local changes in the strain field are strictly related to the presence of microdamage and lacunae in Haversian bone. Nonetheless, the existence of damage was therein assumed a priori, not querying where and when the damage develops and evolves. Moreover, the structural model therein conceived considered, as a simplifying hypothesis, a planar section of the actual three dimensional osteonal structure, thus allowing only for an in-plane strain and stress analysis. In the studies of Guo et al. and Najafi et al., linear elastic fracture mechanics theory was employed to assess the role of microcracks at the level of a single osteon level, as well as their influence on the mechanical behaviour of cortical bone [27, 28]. However, their model revealed several important limitations, since the bone features over multiple length scales were disregarded and the assumptions of two-dimensional plane-strain model and linear elasticity were made. Hamed and Jasiuk numerically investigated the bone strength at multiple length scales by modelling the damage initiation and propagation through the cohesive element technique [18]. The authors provided useful information for understanding bone sub-macroscale failure mechanisms. Nonetheless, several simplifying assumptions were therein made. Specifically, simple material constitutive properties and 2D geometries were

adopted and potential fracture sites were inserted in ad-hoc positions. Moreover, the various scales seem to be decoupled, in the sense that mechanical properties of bone material at a given length scale were obtained not accounting for the bone features and structural organization at lower scales. Giner et al. developed a detailed multiscale model of a single osteon and investigated the microdamage initiation and propagation by employing two different numerical techniques [29]. Therein-obtained numerical results of a radial compressive test, simulating the experimental test carried out by Ascenzi et al. in [30], proved to be in line with the experimental results. However, this loading condition causes only stresses in a plane orthogonal to the osteon axis, which is the reason why the geometry was therein simplified in a 2D half-circular ring and the assumption of plane stress state was made. A model including the three-dimensionality of the osteonal structure and additional constitutive features might be necessary to achieve a thorough understanding of cortical bone microstructural behaviour when different loading conditions are addressed.

Given all previous considerations, this work aims to furnish a novel detailed numerical model of single osteons by accounting for their three-dimensional geometry as well as for several micro- and nano-structural features of cortical bone tissue. More in depth, a refined constitutive description, based on a multistep homogenization procedure, has been developed and employed to characterize the mechanical response of bone material at the osteonal level. A progressive damage formulation has been implemented to model the loss of osteon structural integrity during a whatever loading process. Proposed model has been validated by numerically simulating three different loading scenarios replicating corresponding mechanical tests carried out by Ascenzi and coworkers. Obtained results can provide quantitative indications of cortical bone fracture mechanisms at osteon level. Such results can therefore be useful to enhance the understanding of how microdamage processes and disease- or ageing-induced structural and morphological alterations at each length scale affect the overall mechanical behaviour of cortical bone.

2 Material and Methods

2.1 Problem statement

A typical osteon is regarded as a continuum body lying in the three-dimensional Euclidean space $\mathcal{E}^3$, and whose actual configuration is denoted by Ω. As a notation rule, a subscript (0) appended to the symbol identifying a given quantity will denote that this latter is addressed in the initial configuration. The osteon is assumed as a perfectly cylindrical hollow body, having length L and inner and outer diameter D_H and D_O, respectively (see Fig. 1). As detailed

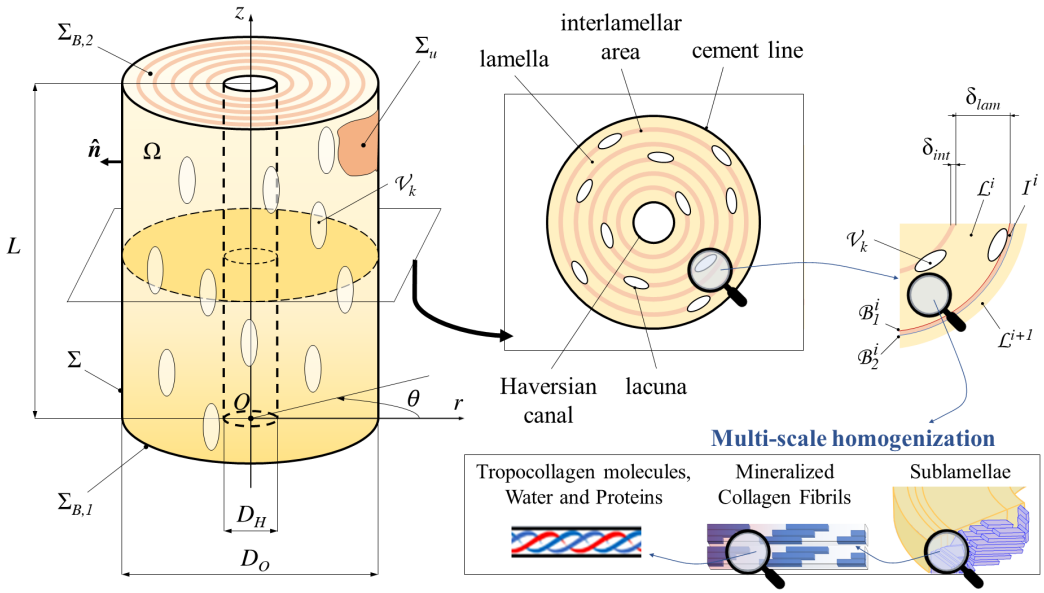

Fig. 1. Schematic of the multiscale model developed illustrating the main geometrical and compositional features of a single osteon, as well as the notation rules.

in the following, the osteon is considered to be made up by a sequence of N coaxially-arranged units, called lamellae, and of $N-1$ very thin interlamellar areas located in between them. Because of this geometrical organization, a cylindrical coordinate system $O\{r,\theta,z\}$ is conveniently introduced. In particular, the origin O is placed at the center of one of the osteon basis and the z-axis coincides with the osteon longitudinal axis, as shown in Fig. 1.

An actual osteonal structure additionally includes lacunae, Volkmann canals, a cement line delimiting the single osteon from the remaining cortical tissue, as well as a fine network of canaliculi (the so-called syncytium). To furnish a detailed mechanical description of the osteonal unit and therefore a thorough understanding of the onset and evolution of microdamage processes within it, it is relevant to account for such microstructural features. Nonetheless, in this work the only presence of lacunae has been considered. This choice follows the approach commonly adopted by other authors, since it is widely accepted that canaliculi and Volkmann canals play a secondary role in comparison to lacunae, due to the greater abundance of these latter [29]. In addition, the influence of cement line becomes significant only if the mechanical behaviour of a set of more than one osteon is addressed, which is not the case herein considered. It is also worth pointing out that the adopted hypotheses are perfectly in-line with the experimental tests carried out by Ascenzi and his coworkers, to which reference is herein made. In fact, the above-mentioned experiments were conducted on single osteons (hence, with no cement line) having a quasi-cylindrical shape accurately selected for the purpose, which

did not show any presence of the Volkmann canals, and from which all the soft tissues were removed [31].

Addressing the generic current configuration Ω, and with reference again to Fig. 1, let symbol $\mathcal{V}^k$ denote the k-th lacunar void domain, $k = 1, \ldots, N_l$, N_l being the total number of lacunae. Let additionally denote with $\mathcal{L}^i$ ($i = 1, \ldots, N$) and $\mathcal{I}^i$ ($i = 1, \ldots, N-1$) the effective geometrical domains, namely accounting for the lacunar voids, occupied by i-th lamella and by the i-th interlamellar area, respectively. Then, by defining domains $\mathcal{L} := \cup_{i=1}^{N} \mathcal{L}^i$ and $\mathcal{I} := \cup_{i=1}^{N-1} \mathcal{I}^i$, the region Ω can be regarded as $\Omega = \mathcal{L} \cup \mathcal{I}$. Moreover, for what follows it is useful to denote with symbols $\mathcal{B}_1^i$, $\mathcal{B}_2^i$ the common interface boundaries between the i-th interlamellar area $\mathcal{I}^i$ and the two subsequent lamellae $\mathcal{L}^i$ and $\mathcal{L}^{i+1}$, respectively, namely $\mathcal{B}_1^i := \mathcal{I}^i \cap \mathcal{L}^i$, $\mathcal{B}_2^i := \mathcal{I}^i \cap \mathcal{L}^{i+1}$ ($i = 1, \ldots, N-1$), and to define domain $\mathcal{B} := \cup_{i=1}^{N-1} (\mathcal{B}_1^i \cup \mathcal{B}_2^i)$. Furthermore, let $\Sigma := \partial\Omega$ be the osteon boundary (comprising the bases, the inner surface of the innermost lamella and the outer surface of the outermost one). In particular, the osteon circular basis at $z = 0$ (at $z = L$, respectively) is denoted with $\Sigma_{B,1}$ ($\Sigma_{B,2}$, resp.). Symbols $\Sigma_p \subseteq \Sigma$ and $\Sigma_u \subseteq \Sigma$ will denote the disjoint and complementary portions of Σ on which tractions $\mathbf{p}$ and displacements $\mathbf{u}_p$ are prescribed in the actual configuration, respectively. By disregarding the volume forces, the unknown actual displacements $\mathbf{u}$, Cauchy stress $\boldsymbol{\sigma}$ and infinitesimal strain $\boldsymbol{\varepsilon}$ fields are obtained by solving the following linearly-elastic problem:

$$\begin{cases} \operatorname{div} \boldsymbol{\sigma} = \mathbf{0} \\ \boldsymbol{\varepsilon} = \nabla^s \mathbf{u} \\ \boldsymbol{\sigma} = \mathbb{C} : \boldsymbol{\varepsilon} \end{cases} \text{ in } \Omega, \text{ with } \begin{cases} \boldsymbol{\sigma}\hat{\mathbf{n}} = \mathbf{p} & \text{on } \Sigma_p \\ \mathbf{u} = \mathbf{u}_p & \text{on } \Sigma_u \end{cases} \tag{1}$$

where $\operatorname{div}(\cdot)$ is the divergence operator, $\nabla^s(\cdot)$ denotes the symmetric part of the gradient operator $\nabla(\cdot)$, $\hat{\mathbf{n}}$ is the outward-pointing normal unit vector to Σ and $\mathbb{C}$ is the tangent fourth-order elastic stiffness tensor at a given material point $P \in \Omega$, which has 21 independent components, owing to its major and minor symmetries.

The osteon is characterized, at the lamellar level, by an anisotropic linearly-elastic constitutive behaviour. Viscous and plasticity effects have been disregarded, whereas the bone tissue typical brittle behaviour has been taken into account by means of a damage mechanics-based modelling. As better clarified in the following, the progressive loss of the osteon structural integrity induced by cracks nucleation and propagation is accounted for, so that tensor $\mathbb{C}$ depends also on the stress state in the actual configuration.

2.2 Multiscale constitutive rationale

The constitutive behaviour of the osteonic lamellar tissues is modelled in the framework of a multiscale approach. Starting from the nanoscale level, a multi-step homogenization procedure is implemented to obtain the anisotropic and locally-homogeneous equivalent elastic properties of the osteon. The procedure is detailed in the following.

2.2.1 Nanoscale: mineralized collagen fibrils

The basic building blocks of cortical bone at the nanoscale level are Type-I collagen, hydroxyapatite (HA) crystals and small quantities of water and non-collagenous proteins (NCPs), which together form the so-called mineralized collagen fibrils (MCFs). These latter result from a mineralization process of simple collagen fibres, which are made up of staggered tropocollagen molecules having length equal to $\ell_c = 300\,\text{nm}$ (in unmineralized conditions), and exhibiting a well-known along-the-length periodicity value of $\lambda = 67\,\text{nm}$ as well as $\lambda_G = 40\,\text{nm}$-long gap regions between the ends of two successive molecules. Such an arrangement, known as the Hodge-Petruska scheme, is sketched in Fig. 2(a) [9, 32]. As proved by well-established histological evidence, the mineralization process consists in the progressive growth of HA crystals within the gap regions [9, 33]. As a result, the mineral phase is arranged in a staggered way within a water-protein-collagen (WPC) matrix, which gives to compact bone a peculiar combination of stiffness and toughness. The shape of mature HA crystals is generally rather irregular, but many investigations showed that they are for most platelet-shaped [11, 33, 34].

On account of the spatial organization of bone nanoconstituents, and by following an approach similar to [29, 35, 36], MCFs are modelled as a composite material in which the reinforcement phase, represented by the HA platelets, is embedded in a staggered manner within a water-protein-collagen matrix, as shown in Fig. 2(b). By introducing a local reference system $\{\mathbf{e}_1, \mathbf{e}_2, \mathbf{e}_3\}$, with the $\mathbf{e}_3$-axis aligned to the collagen fibrils axis, and for what stated in the foregoing, the mineral phase platelets have been assumed as parallelepipedic, with linear dimensions along the $\mathbf{e}_1$, $\mathbf{e}_2$ and $\mathbf{e}_3$ axes equal to d_{HA}, b_{HA} and ℓ_{HA}, respectively. Moreover, the along-the-width and along-the-depth lateral spacing between two subsequent HA crystal platelets will be denoted with symbols Δd and Δb, respectively.

The mineral phase is assumed as an isotropic linearly-elastic material, characterized by an elastic stiffness tensor $\mathbb{C}_{HA}$ dependent on Young's modulus E_{HA} and Poisson's ratio ν_{HA}. On the other hand, the WPC matrix has been in turn regarded as a composite material made up by perfectly-aligned tropocollagen

long fibres, having volume fraction Φ'_c, embedded in a water-protein matrix (with volume fraction $\Phi'_{wp} = 1 - \Phi'_c$). It is worth noting that the elasticity of the water-protein matrix arises by hydrogen bonds linking the collagen molecules as well as by crosslinks provided by the NCPs [37]. Then again, sub-nanoscale organizations, features and mechanisms typical of collagen (as the energetic and entropic mechanisms described e.g. in [38]) have been disregarded due to both the big difference in stiffness between the WPC matrix and mineral phase and to the great abundance of this latter. In fact, for high values of mineral volume fraction, which are distinctive of a healthy bone tissue, the typical so-called "toe" and "heel" parts of the characteristic stress-strain curve of collagen tend to disappear, so that sub-nanoscale features of collagen might have a negligible impact on the outcomes for bone tissue [33, 35]. Both phases of the WPC matrix are assumed to be isotropic linearly-elastic. On the other hand, due to the geometrical organization of tropocollagen molecules, WPC composite shows a transversely-isotropic elastic symmetry with respect to the plane $\{\mathbf{e}_1, \mathbf{e}_2\}$ orthogonal to the collagen molecules axis. The equivalent five elastic constants characterizing the WPC mechanical response have been obtained analytically. In detail, let symbols E_{ph} and ν_{ph} denote the Young's modulus and Poisson's ratio, respectively, of phase $ph \in \{wp, c\}$, where subscripts wp and c refer to the water-protein matrix and to the tropocollagen molecules, respectively. Moreover, let G_{ph} and k_{ph} be the plane-strain shear and bulk moduli of phase ph, respectively defined for an isotropic material as:

$$G_{ph} := \frac{E_{ph}}{2\,(1+\nu_{ph})} \tag{2a}$$

$$k_{ph} := \frac{5-4\nu_{ph}}{6\,(1-2\nu_{ph})\,(1+\nu_{ph})}\,E_{ph} \tag{2b}$$

Then, the equivalent shear and bulk moduli of WPC composite $G_{WPC,12}$ and $k_{WPC,12}$ in the plane $\{\mathbf{e}_1, \mathbf{e}_2\}$ have been computed through the following expressions [37, 39]:

$$G_{WPC,12} = G_{wp}\left(\frac{1 + k_{wp}\,\mu'\,\Phi'_c - F_\xi - F_\eta}{1 - (k_{wp}+2G_{wp})\,\mu'\,\Phi'_c - F_\xi - F_\eta}\right) \tag{3a}$$

$$k_{WPC,12} = k_{wp}\left(\frac{1 + G_{wp}\,\kappa'\,\Phi'_c - 2F_\xi}{1 - k_{wp}\,\kappa'\,\Phi'_c - 2F_\xi}\right) \tag{3b}$$

where by definition:

$$\begin{aligned} F_\xi &:= k_{wp}\,G_{wp}\,\mu'\,\kappa'\,\Phi'_{wp}\,\xi & F_\eta &:= k_{wp}^2\,\mu'^2\,\Phi'_{wp}\,\eta \\ \kappa' &:= \tfrac{k_c - k_{wp}}{k_{wp}\,(k_c + G_{wp})} & \mu' &:= \tfrac{G_c - G_{wp}}{k_{wp}\,G_{wp} + (k_{wp}+2G_{wp})\,G_c} \end{aligned} \tag{4}$$

and ξ, η are scalar parameters defined by threefold integrals numerically computed in [40, 41]. The equivalent longitudinal Young's modulus $E_{WPC,33}$ and Poisson's ratio $\nu_{WPC,33}$ have been obtained by employing Hill's lower-bound estimates for fiber-reinforced composites [42]:

$$E_{WPC,33} = \Phi'_{wp} E_{wp} + \Phi'_c E_c + \frac{4\Phi'_{wp}\Phi'_c(\nu_{wp} - \nu_c)^2}{\frac{\Phi'_{wp}}{k_c} + \frac{\Phi'_c}{k_{wp}} + \frac{1}{G_c}} \tag{5a}$$

$$\nu_{WPC,33} = \Phi'_{wp}\nu_{wp} + \Phi'_c\nu_c + \frac{\Phi'_{wp}\Phi'_c(\nu_{wp} - \nu_c)\left(\frac{1}{k_{wp}} + \frac{1}{k_c}\right)}{\frac{\Phi'_{wp}}{k_c} + \frac{\Phi'_c}{k_{wp}} + \frac{1}{G_c}} \tag{5b}$$

The remaining elastic constant, e.g. the longitudinal shear modulus $G_{WPC,13}$, has been estimated as $G_{WPC,13} \simeq 1.04\, G_{WPC,12}$, according to [37]. From $G_{WPC,12}$, $k_{WPC,12}$, $E_{WPC,33}$, $\nu_{WPC,33}$ and $G_{WPC,13}$ it is relatively straightforward to compute the equivalent stiffness tensor $\mathbb{C}_{WPC}$ of WPC matrix.

Thereby, by employing the geometrical and constitutive parameters introduced in this Section, the MCFs equivalent elastic stiffness tensor $\mathbb{C}_{MCF}$ is obtained as a result of a numerical homogenization step, whose details are reported in Section 2.4.1.

2.2.2 Microscale: single lamellae

As clearly proved by many evidence, the single lamellar unit is made up of $N_s = 5$ adjacent sublayers (or sublamellae). In turn, each sublamella is constituted by bundles of MCFs roughly parallel to each other, but having different orientations in the different sublayers, giving rise to the so-called rotated-twisted-plywood structure [13, 14]. Accordingly, the MCFs' orientation in the j-th sublayer ($j = 1, \ldots, N_s$) of the i-th lamella ($i = 1, \ldots, N$), with respect to the osteon long axis z, can be uniquely characterized by two angles χ^i_j and ψ^i_j, [13, 43]. In particular, as sketched in Fig. 2(c)-(d), by introducing a local orthogonal reference system $\{r^*, r^*_\perp, z^*\}$, r^* and $r^*_\perp$ being the local radial and circumferential direction at angle $\theta = \theta^*$, respectively, χ^i_j is the plywood angle, namely the rotation angle of the MCFs around r^*, whereas ψ^i_j is the rotation angle around $r^*_\perp$ [11].

Let us consider the i-th lamella constituting the osteonal structure, having internal and external radii r^i_{int} and r^i_{ext}, respectively. If δ^i_j denotes the thickness of the j-th sublayer within the i-th lamella, the thickness of i-th lamella results:

$$\delta^i_{lam} = r^i_{ext} - r^i_{int} = \sum_{j=1}^{N_s} \delta^i_j \tag{6}$$

The elastic stiffness tensor $\mathbb{C}_j^i$ of the j-th sublayer within the i-th lamella in the global cylindrical reference system is obtained by transforming the components of tensor $\mathbb{C}_{MCF}$ from the $\{\mathbf{e}_1, \mathbf{e}_2, \mathbf{e}_3\}$ reference system to the $O\{r, \theta, z\}$ one by means of two transformation tensors, $\mathbb{T}_j$ and $\mathbb{D}_j$, according to the following relationship [44]:

$$\mathbb{C}_j^i = \mathbb{T}_j \, \mathbb{C}_{MCF} \, \mathbb{D}_j^{-1} \tag{7}$$

The matricial form of transformation tensors $\mathbb{T}_j$ and $\mathbb{D}_j$, which depend on angles χ_j^i and ψ_j^i, is reported in the Appendix for the sake of completeness and readability. It is remarked that, following well-established evidence, angles χ_j^i and ψ_j^i, as well as the thickness δ_j^i of the single sublamella are supposed to be the same for each lamella [11,13,43]. Therefore, it results $\chi_j^i = \chi_j$, $\psi_j^i = \psi_j$, $\delta_j^i = \delta_j$, and $\delta_{lam}^i = \delta_{lam}$ for each $i = 1, \ldots, N$.

A further numerical homogenization step allows to reduce the lamellar tissue to an equivalent completely anisotropic and locally-homogeneous linearly-elastic material, described in the reference configuration by the fourth-order elastic stiffness tensor $\mathbb{C}_{lam,(0)}^i$. It is worth observing that, as a consequence of the previous positions, it results $\mathbb{C}_{lam,(0)}^i = \mathbb{C}_{lam,(0)}$ for each $i = 1, \ldots, N$.

2.2.3 Sub-macroscale: osteon tissues

As previously mentioned, the osteon has been considered as a hollow cylindrical structure made up (in the initial configuration) of N concentric lamellae having their common long axis coincident to the z-axis. From a constitutive viewpoint, every point belonging to each osteonal lamella in the reference configuration has been characterized by the previously-introduced tensor $\mathbb{C}_{lam,(0)}$.

Between two subsequent lamellae, a very thin and weak interface zone exist, known as interlamellar area [45]. In this work, all the interlamellar areas are assumed to have the same thickness δ_{ia}. As stated by Rho et al. [9], the real composition of the interlamellar zones has still to be fully elucidated, but it seems that they result particularly rich in NCPs (primarily osteocalcin and osteopontin) and randomly-oriented collagen molecules [12, 46]. Nonetheless, such interfaces appear to have significant contributions on the mechanical behaviour of single osteons [45]. In particular, as a first approximation due to the lack of knowledge on the topic, the interlamellar areas have been considered as isotropic linearly-elastic materials. As such, their fourth-order elastic stiffness tensor in the reference configuration $\mathbb{C}_{ia,(0)}$ is fully characterized by the Young's modulus E_{ia} and the Poisson's ratio ν_{ia}. Owing to their small thickness, the interlamellar areas have been modelled as thin elastic layers, as better clarified in Section 2.4.1.

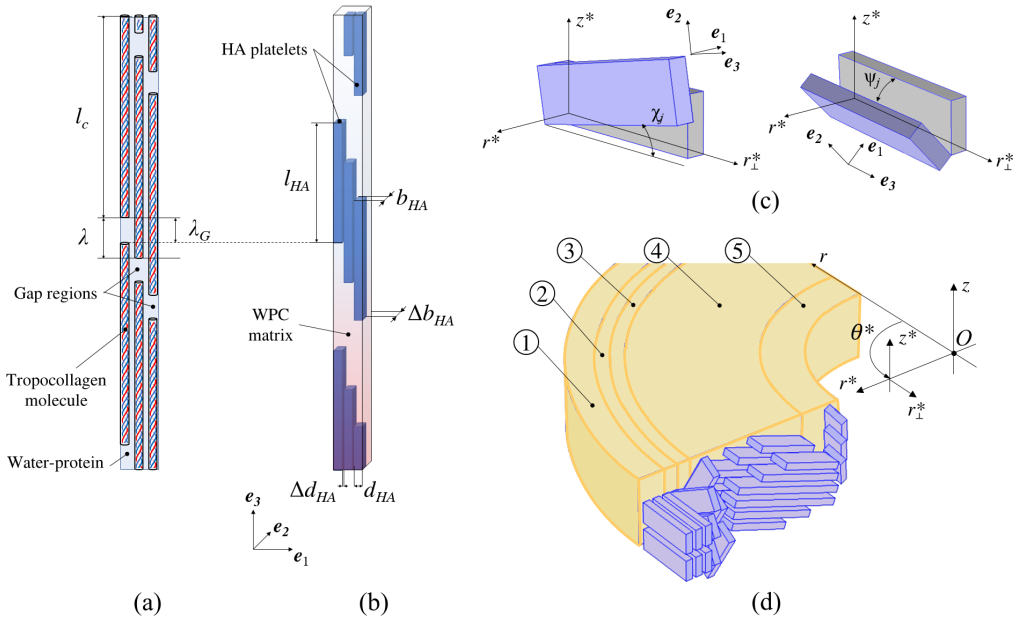

Fig. 2. The Mineralized Collagen Fibrils (MCFs) and their arrangement within the lamellar structure. (a) The Hodge-Petruska scheme describing the geometrical organization of tropocollagen molecules immersed in a water-protein matrix. (b) Platelet-shaped HA crystals lie within the gap regions originating from the collagen staggered alignment. (c) Angles of rotation χ_j and ψ_j of MCFs with respect to the local reference system $\{r^*, r^*_\perp, z^*\}$. (d) MCFs arrangement within the five sublayers constituting a typical osteonic lamella.

The presence of lacunae, very important feature to assess and predict the real stress distribution within the osteonal structure, has also been accounted for. Lacunae are small cavities hosting the osteocytes (i.e., quiescent osteoblasts, these latter being the cells secreting the osteonal tissue), and which are mainly located at the interlamellar interfaces level [16]. Following the evidence reported in [47], their shape can be considered as approximately ellipsoidal, with principal axes that will be denoted, from the longest to the shortest, as a, b and c. In particular, the minor axis c lies in a plane orthogonal to the longitudinal z-axis of the osteon, and the major axis is roughly parallel to the z-axis [48]. In this work, this description has been adopted for each lacunar cavity present in the osteon. The number of lacunae N_l is chosen such that their volume fraction f_l within a typical osteon lies in the range $1 \div 3\%$, which is a representative value for mature and healthy cortical tissue [16]. Lacunar voids volume fraction f_l is then readily computed as:

$$f_l = \frac{N_l \, |\mathcal{V}^k_{(0)}|}{|\tilde{\Omega}_{(0)}|} = \frac{16 \, N_l \, a \, b \, c}{3 \, (D_O^2 - D_H^2) \, L} \tag{8}$$

where symbol $|\bullet|$ denote the measure of domain $\bullet$, and $\mathcal{V}^k_{(0)}$, $\tilde{\Omega}_{(0)}$ are, respectively, the domain occupied by the k-th lacunar void and the one occupied

by the osteon in the initial configuration if lacunae were absent, i.e. such that $\tilde{\Omega}_{(0)} = \left[\frac{D_H}{2}, \frac{D_O}{2}\right] \times [0, 2\pi] \times [0, L]$ in the global cylindrical coordinate system.

2.3 Failure criteria and damage law

To describe the mechanical behaviour of a single osteon up to the failure state, thus accounting for its progressive loss of structural integrity due to loading-induced nucleation and propagation of microcracks, all osteonic tissues at the sub-macroscale level are considered as perfectly brittle materials. Therefore, by adopting a stress-based damage description, failure in a material point $P \in \Omega$ occurs when

$$F(\boldsymbol{\sigma}) \geq 1 \tag{9}$$

where $F(\boldsymbol{\sigma})$ is a scalar-valued function dependent on the actual local stress state and expressing a suitable failure criterion.

Since a typical osteon can be conceived as a multi-layered composite material, two distinct failure modes have been distinguished, i.e. an interlaminar failure and an intralaminar one. The former, occurring at the interlamellar areas level, is caused by delamination between two successive osteonic lamellae, whereas the latter occurs in the bulk. As such, two distinct functions F, depending on the material point position $P \in \Omega$, have been adopted to model local failure conditions, namely:

$$F(\boldsymbol{\sigma}) = \begin{cases} F_{lam}(\boldsymbol{\sigma}) & \text{if } P \in \mathcal{L} \setminus \mathcal{B} \\ F_{ia}(\boldsymbol{\sigma}) & \text{if } P \in \mathcal{I} \end{cases} \tag{10}$$

In detail:

- for the interlaminar failure mode ($P \in \mathcal{I}$), following [29], the quadratic Brewer-Lagacé criterion is adopted. In this case only the σ_{rr}, $\sigma_{r\theta}$ and σ_{rz} components of the stress tensor $\boldsymbol{\sigma}$ contribute to failure and function $F = F_{ia}$ reads as [49]:

$$F_{ia}(\boldsymbol{\sigma}) = \left(\frac{\langle \sigma_{rr} \rangle_+}{S_{rr}}\right)^2 + \left(\frac{\sigma_{r\theta}}{S_{r\theta}}\right)^2 + \left(\frac{\sigma_{rz}}{S_{rz}}\right)^2 \tag{11}$$

  In Eq. (11), symbol $\langle \circ \rangle_+ = \max\{0, \circ\}$ denotes the positive part of $\circ$, and S_{rr}, $S_{r\theta}$ and S_{rz} represent some tensile and shear strength parameters of the interfaces. It is worth pointing out that the positive part function prevents the occurrence of damage in compressive regions. In fact, damage

usually propagates much more easily in tension than in compression, and therefore, as a first approximation, damage caused by compressive stresses has been disregarded.

- for the intralaminar failure mode ($P \in \mathcal{L} \setminus \mathcal{B}$), the Von Mises criterion is adopted. Accordingly, by denoting with $\boldsymbol{s}$ the stress deviator tensor, function $F = F_{lam}$ reads as:

$$F_{lam}(\boldsymbol{\sigma}) = \frac{\sqrt{\frac{3}{2}\mathrm{tr}(\boldsymbol{s}^2)}}{S_{lam}} \tag{12}$$

S_{lam} being a strength parameter for the lamellar bulk tissue.

When the failure condition is locally detected, a local degradation of the tissue elastic properties is enforced, in accordance with the Continuum Damage Mechanics theory. As a consequence, tensor $\mathbb{C} = \mathbb{C}(P, \boldsymbol{\sigma})$ appearing in Eq. (1) results as:

$$\mathbb{C}(P, \boldsymbol{\sigma}) = \begin{cases} \mathbb{C}_{lam}(\boldsymbol{\sigma}) & \text{if } P \in \mathcal{L} \setminus \mathcal{B} \\ \mathbb{C}_{ia}(\boldsymbol{\sigma}) & \text{if } P \in \mathcal{I} \end{cases} \tag{13}$$

Owing to the bone tissue brittleness at the sub-macroscale level, as a simple and effective degradation rule, all the components of the elastic stiffness tensor $\mathbb{C}$ are made to vanish when failure conditions are locally detected.

2.4 Numerical treatment

2.4.1 Multiscale homogenization procedure

The multi-step homogenization procedure described in Section 2.2 has been implemented through customized codes in Matlab environment (Matlab v. R2018a, MathWorks, MA, USA) integrated within the FE solver Comsol Multiphysics (Comsol with Matlab, v.5.4 COMSOL, Stockholm, Sweden).

At the nanoscale level, the equivalent properties of a single MCF are obtained by assuming the staggered arrangement of mineral platelets previously illustrated (see Fig. 2(b)). In particular, by defining the quantities $d_f := d_{HA} + \Delta d$ and $b_f := b_{HA} + \Delta b$, to obtain the MCFs homogenized elastic stiffness tensor $\mathbb{C}_{MCF}$, a Representative Unit Cell (RUC) having edge lengths along the $\mathbf{e}_1$, $\mathbf{e}_2$ and $\mathbf{e}_3$ axes equal to $10d_f$, b_f and $2\ell_f$, respectively, has been chosen, as illustrated in Fig 3(a). The volume fraction of HA platelets within the MCFs,

Table 1
Vaules of the nano-scale model parameters employed in the numerical simulations.

Nanoscale (MCFs)			
Parameter	**Symbol**	**Value**	**References**
Degree of mineralization	Φ [%]	40	[35, 50]
Water-protein volume fraction	Φ_{wp} [%]	13	[51]
Tropocollagen molecules undeformed length	ℓ_c [nm]	300	[32, 33]
Gap region length	λ_G [nm]	40	[9, 32]
HA platelets width	d_{HA} [nm]	3	[9, 17, 33]
HA platelets depth	b_{HA} [nm]	25	[9, 17, 33]
Along-the-width spacing between HA platelets	Δd [nm]	1	[36, 52]
Along-the-depth spacing between HA platelets	Δb [nm]	3	[36, 52]
Collagen Young's modulus	E_c [GPa]	2	[37, 53, 54]
Collagen Poisson's ratio	ν_c [−]	0.28	[51, 55]
Water-protein Young's modulus	E_{wp} [GPa]	0.29	[37]
Water-protein Poisson's ratio	ν_{wp} [−]	0.49	[37]
HA platelets Young's modulus	E_{HA} [GPa]	114	[56, 57]
HA platelets Young's modulus	ν_{HA} [−]	0.27	[56]
Parameter ξ	ξ [−]	0.016	[40]
Parameter η	η [−]	0.420	[41]

also known as the degree of mineralization of cortical tissue, thereby results:

$$\Phi = \frac{\ell_{HA}}{\ell_f} \cdot \frac{b_{HA}}{b_f} \cdot \frac{d_{HA}}{d_f} \tag{14}$$

As a consequence, by denoting with Φ_{wp} and Φ_c the volume fractions of water-protein and collagen within MCFs (i.e., satisfying the condition $\Phi_{wp}+\Phi_c+\Phi = 1$), the volume fractions Φ'_{wp} and Φ'_c of water-protein and collagen within the WCP composite matrix, employed in Eqs. (3),(5), can be evaluated as:

$$\Phi'_{wp} = \frac{\Phi_{wp}}{\Phi_{wp} + \Phi_c} \tag{15a}$$

$$\Phi'_c = \frac{\Phi_c}{\Phi_{wp} + \Phi_c} \tag{15b}$$

Table 2
Vaules of the micro-scale model parameters employed in the numerical simulations.

Microscale (Single lamellae)							
Parameter	**Symbol**	**Value(s)**					**References**
Number of sublamellae	N_s	5					[14, 36]
Sublamella index	j	1	2	3	4	5	
MCFs plywood angle	χ_j [°]	0	30	60	90	120	[13, 58]
MCFs rotation angle	ψ_j [°]	0	0	0	70	30	[13, 58]
Sublamella thickness	δ_j [µm]	0.6	1.8	0.2	0.2	0.4	[43]
Lamella thickness	δ_{lam} [µm]	3.2					Eq. (6)

By noting that $\ell_f = \ell_c + \lambda_G$, for a given Φ the corresponding crystal length ℓ_{HA} can be derived from Eq. (14), having considered all the other quantities as given. It is worth pointing out that the assumed values of Φ and the corresponding ℓ_{HA} values lie within the commonly observed range of variability reported by several authors [35, 50, 52, 59]. All values of geometric and constitutive parameters for both MCFs and sublamellar structures, chosen in agreement with literature data, are summarized in Tables 1 and 2, respectively.

Second-order displacement-based tetrahedral elements with average size $h_{MCF} = \frac{d}{3}$ have been adopted to generate the computational mesh (see Fig. 3(a)) In the second homogenization step, the equivalent elastic stiffness tensor of each lamella $\mathbb{C}_{lam}$ has been computed by employing a cubic RUC with an edge size equal to δ_{lam} and a structured mesh consisting in second-order brick elements

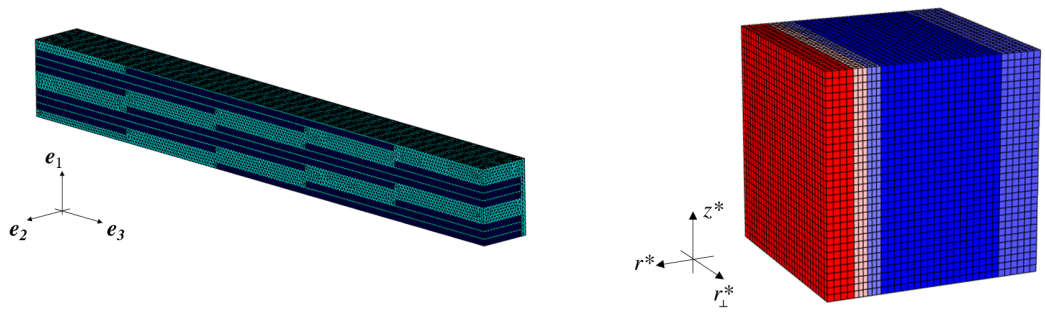

(a) (b)

Fig. 3. Representative Unit Cells employed in the two-step numerical homogenization procedure to obtain the equivalent elastic properties of (a) MCFs and (b) lamellar tissue. The discretization adopted in both cases is also shown.

Table 3
Vaules of the model parameters at the osteon level employed in the numerical simulations.

Sub-macroscale (Single osteon)			
Parameter	**Symbol**	**Value(s)**	**References**
Osteon inner diameter (Haversian canal diameter)	D_H [µm]	40.0	[31, 62, 63]
Osteon outer diameter	D_O [µm]	210.4	[31, 62, 63]
Osteon length	L [µm]	500.0	[31, 62, 63]
Number of lamellae	N [−]	26	Eq. (16)
Lacunae dimensions	$a \times b \times c$ [µm × µm × µm]	22×9×4	[16, 47]
Lacunae volume fraction	f_l [%]	2.1	[16]
Number of lacunae	N_l [−]	104	Eq. (8)
Interlamellar area thickness	δ_{ia} [µm]	0.08	[46]
Interlamellar area Young's modulus	E_{ia} [GPa]	3	[45]
Interlamellar area Poisson's ratio	ν_{ia} [−]	0.3	[45]
Interface radial tensile strength parameter	S_{rr} [MPa]	40	[29, 64, 65]
Interface circumferential debonding shear strength	$S_{r\theta}$ [MPa]	25	[29, 64, 65]
Interface axial debonding shear strength	S_{rz} [MPa]	25	[64, 65]
Lamellar bulk strength	S_{lam} [MPa]	120	[66]

all having an edge dimension equal to $h_{lam} = \frac{1}{3} \min_j \delta_j$, as shown in Fig. 3(b). Previous mesh element sizes have been chosen as a result of a preliminary convergence analysis. To enhance the estimate of the elastic constitutive tensors $\mathbb{C}_{MCF}$ and $\mathbb{C}_{lam}$, and in accordance with the composite homogenization theory, displacement-based Periodic Boundary Conditions have been enforced on the external faces of the RUCs for both homogenization steps [60, 61].

2.4.2 Osteon micromechanical behaviour

Table 3 lists all geometrical and constitutive parameters characterizing a single osteon, together with their respective values employed in the numerical simulations. In particular, under the hypotheses of the present model, D_O and D_H, known from the experiments, are related to the number of lamellae N through the following relationship:

$$\frac{D_O - D_H}{2} = N\,\delta_{lam} + (N-1)\,\delta_{ia} \tag{16}$$

Therefore, for a given D_H, N is chosen as an integer number such that the osteon outer diameter D_O, computed through Eq. (16), lies in the range of values employed in the actual experiments.

Following an approach similar to the one adopted in [67], the i-th interlamellar area is numerically treated as a discrete elastic interface joining two subsequent osteonic lamellae, due to its very small thickness. In particular, the mechanical response of the interlamellar areas is described by a distribution of linearly-elastic 3D springs connecting each pair of nodes belonging to the interface boundaries $\mathcal{B}_1^i$ and $\mathcal{B}_2^i$. As a consequence, the elastic properties of region $\mathcal{I}^i$ are fully characterized by two parameters K_n and K_t describing normal- and tangential-to-surface stiffness interactions, respectively. K_n and K_t depend on the interlamellar areas elastic constants E_{ia}, ν_{ia} and thickness δ_{ia}, according to the following expressions:

$$K_n = \frac{E_{ia}\,(1-\nu_{ia})}{(1+\nu_{ia})\,(1-2\nu_{ia})\,\delta_{ia}} \tag{17a}$$

$$K_t = \frac{E_{ia}}{2\,(1+\nu_{ia})\,\delta_{ia}} \tag{17b}$$

It is worth remarking that, due to the definition of K_n and K_t, the nodal reactions exhibited by the springs are forces per unit area (namely, stresses). Accordingly, the local stress tensor needed to assess potential local interlaminar failure conditions can be straightforwardly computed.

The developed multiscale model has been validated by replicating in a numerical framework three distinct loading scenarios corresponding to three different mechanical experiments performed on single osteons by Ascenzi and his coworkers. Characteristic dimensions at the sub-macroscale level of both osteonic geometry and loading zones replicate the ones actually adopted in the mechanical tests. The experiments considered in this paper concern a tensile test [62], a torsion test [63] and a three-point bending test [31], which in the following will be referred to as the T-, Θ-, and B-tests, respectively. It is important to highlight that, with the view of reducing the demanding computational cost of numerical simulations, and due to the geometrical quasi-symmetry of the structure, a quarter of total domain Ω, suitably chosen according to the particular loading condition addressed, has actually been modelled, as detailed below. To faithfully mimic the experiments, suitable boundary conditions have been enforced in each case. Specifically, by referring to Fig. 4:

- In the T-test, the only portion $\Omega' \subset \Omega$ such that $\theta \in I_\theta := [0, \frac{\pi}{2}]$ is considered. Accordingly, $\Sigma'_{B,1}$ and $\Sigma'_{B,2}$, which are the restrictions of $\Sigma_{B,1}$ and $\Sigma_{B,2}$ on I_θ respectively, result as the effectively-modelled bases. Moreover, by denoting with $\mathcal{P}_\theta$ ($\theta \in [0, 2\pi)$) the θ-half-plane having the z-

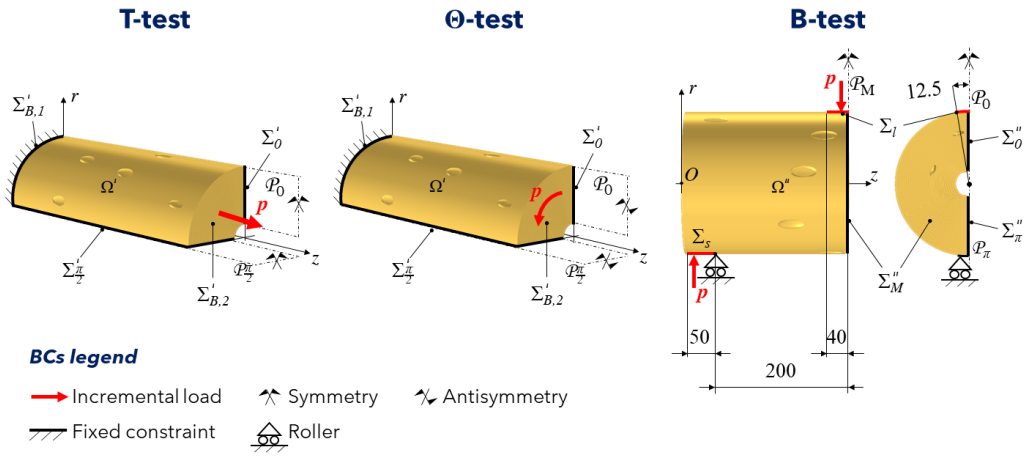

Fig. 4. Applied boundary conditions for the three investigated loading scenarios. From left to right: tension test, torsion test and three-point bending test. Dimensions in the bending test sketch corresponds to the ones actually employed in the experiments and are given in micrometers.

axis as origin and forming an angle θ with the rz-half-plane, two new osteon boundary surfaces can be identified, that is $\Sigma'_0 := \Omega' \cap \mathcal{P}_0$ and $\Sigma'_{\frac{\pi}{2}} := \Omega' \cap \mathcal{P}_{\frac{\pi}{2}}$. In the T-test, $\Sigma_u \equiv \Sigma'_{B,1} \cup \Sigma'_0 \cup \Sigma'_{\frac{\pi}{2}}$: the osteon has been fully constrained ($\mathbf{u} = \mathbf{0}$) on $\Sigma'_{B,1}$, whereas symmetry conditions ($\mathbf{u} \cdot \hat{\mathbf{n}} = \mathbf{0}$) have been enforced on $\Sigma'_0 \cup \Sigma'_{\frac{\pi}{2}}$. An incremental longitudinal load $\mathbf{p}$ distributed upon $\Sigma'_{B,2}$ has been additionally applied.

- In the Θ-test, the portion Ω' has been again considered, so that the boundaries Σ_u and Σ_p, as well as the osteon geometrical symmetry planes, are the same of those employed in the T-test. On the other hand, in this case, an incremental circumferential load is enforced on $\Sigma'_{B,2}$ and antisimmetry conditions (described by the condition $\mathbf{u} \cdot \hat{\mathbf{t}} = \mathbf{0}$, $\hat{\mathbf{t}}$ denoting a general tangential direction to Σ'_0 or $\Sigma'_{\frac{\pi}{2}}$) have been imposed on $\Sigma'_0 \cup \Sigma'_{\frac{\pi}{2}}$. Boundary $\Sigma'_{B,1}$ has been fully constrained.
- In the B-test, the only portion $\Omega'' \subset \Omega$ such that $\theta \in [0, \pi]$ and $z \in [0, \frac{L}{2}]$ is actually modelled. As a result, by denoting with $\mathcal{P}_M$ the plane of equation $z = \frac{L}{2}$, three new osteon boundaries $\Sigma''_0 := \Omega'' \cap \mathcal{P}_0$, $\Sigma''_\pi := \Omega'' \cap \mathcal{P}_\pi$ and $\Sigma''_M := \Omega'' \cap \mathcal{P}_M$ can be identified. In this case, opposite and equal incremental loads have been applied on portions $\Sigma_l \subset \Sigma$ and $\Sigma_s \subset \Sigma$ respectively corresponding to the loaded region and to the free support zone in the actual three-point bending experiment. The dimensions of such zones are equal to the ones adopted in [31] and are synthetically reported in the sketch in Fig. 4. Simple support and symmetry conditions have been enforced on the edge of Σ_s closer to Σ_M and on $\Sigma''_0 \cup \Sigma''_\pi \cup \Sigma''_M$, respectively.

Second-order displacement-based tetrahedral elements have been employed to

Table 4
Type and values of incremental loading applied in the numerical simulations for the T-, Θ-, and B-tests. The deformation parameter evaluated in each case is also reported.

Loading increments			
Mechanical test	**Type of applied loading**	**Value**	**Deformation parameter evaluated**
T-test	Incremental force per unit area p [MPa]	5.0000	Elongation [%]
Θ-test	Incremental torque T [$\times 10^{-5}$ N m]	1.4955	Angle of twist [crad]
B-test	Incremental force F [N]	0.1226	Deflection [μm]

discretize the osteon geometrical domain Ω_0. The average mesh element size has been set equal to $h = \frac{1}{2}\delta_{lam}$, thereby generating unstructured meshes having about 6.500.000 elements and 27 millions degrees of freedom.

The progressive damage within the osteonal structure is simulated by implementing a numerical iterative procedure through customized codes developed in Matlab environment, additionally exploiting FE solver-core libraries of Comsol Multiphysics. Post-processing phases have been performed in both applications. It is important to preliminarly observe that, to avoid spurious mesh sensitivity of the results deriving from the local damage approach, a regularization technique similar to the one described in [MIO] has been implemented. Starting from the discretized model of the osteon in the reference configuration, the undamaged anisotropic constitutive properties are assigned. The loading process consists in a sequence of equal loading increments enforced on the previously-introduced boundary surfaces, whose values are reported in Table 4. Once the solution of linearly-elastic problem (Eq. (1)) is computed at a given computational step, the actual value of stress field $\boldsymbol{\sigma}$ is evaluated at each mesh Gauss point and employed to compute functions F_{ia}, F_{lam} described by Eqs. (11) and (12), respectively. If local failure occurs nowhere in Ω, namely conditions $F_{ia}(\boldsymbol{\sigma}) < 1$ and $F_{lam}(\boldsymbol{\sigma}) < 1$ contemporary hold for each Gauss point, the algorithm evaluates a proper deformation parameter depending on the particular loading condition addressed (see Table 4), and updates the material properties for the successive loading step. On the contrary, if local failure conditions are detected, the same displacement step is iteratively repeated until further variations in the damage pattern are no longer revealed. Such an approach ensures the stress redistribution in the neighbourhood of the failed zone (i.e., equilibrium condition), as well as the compatibility of each incremental solution. When the algorithm fails to find convergence conditions, the osteon is assumed to be completely failed.

3 Results and discussion

3.1 Preliminary results: obtained homogenized stiffness tensors

For completeness, in the following are briefly reported the homogenized elastic stiffness tensors $\mathbb{C}_{MCF}$, $\mathbb{C}_{lam}$ computed via the multiscale homogenization procedure described in Sections 2.2.1 and 2.2.2, and by employing values of model parameters listed in Tables 1 and 2.

$$\mathbb{C}_{MCF}\ [\text{GPa}] = \begin{bmatrix} 4.676 & 1.621 & 2.006 & 0 & 0.004 & 0 \\ 1.621 & 13.531 & 3.792 & 0.003 & -0.057 & 0 \\ 2.006 & 3.792 & 40.523 & 0.006 & -0.952 & 0 \\ 0 & 0.003 & 0.006 & 4.079 & 0 & -0.073 \\ 0.004 & -0.057 & -0.952 & 0 & 1.287 & 0 \\ 0 & 0 & 0 & -0.073 & 0 & 1.152 \end{bmatrix} \tag{18}$$

$$\mathbb{C}_{lam}\ [\text{GPa}] = \begin{bmatrix} 8.523 & 2.957 & 2.607 & 0.111 & -1.646 & -0.072 \\ 2.957 & 32.252 & 4.571 & -1.137 & -0.442 & -0.292 \\ 2.607 & 4.571 & 12.522 & 0.070 & -0.583 & -0.061 \\ 0.111 & -1.137 & 0.070 & 4.312 & -0.101 & -0.695 \\ -1.646 & -0.442 & -0.583 & -0.101 & 2.091 & 0.097 \\ -0.072 & -0.292 & -0.060 & -0.695 & 0.097 & 2.832 \end{bmatrix} \tag{19}$$

3.2 Osteon micromechanical behaviour

In the following, FE-based predictions of the osteon mechanical behaviour obtained by employing the previously-described multiscale approach are detailed. For each numerically-addressed loading condition, obtained results are compared to the corresponding experimental ones available in the literature. In particular, reference is made to [62],[63],[31] for the T-, Θ and B-test, respectively. Numerical results are provided in terms of:

- plots of applied load vs. the related deformation parameter (see Table 4);
- osteon moduli of elasticity, as well as load and deformation values at failure state, namely at the last step of numerical convergence;

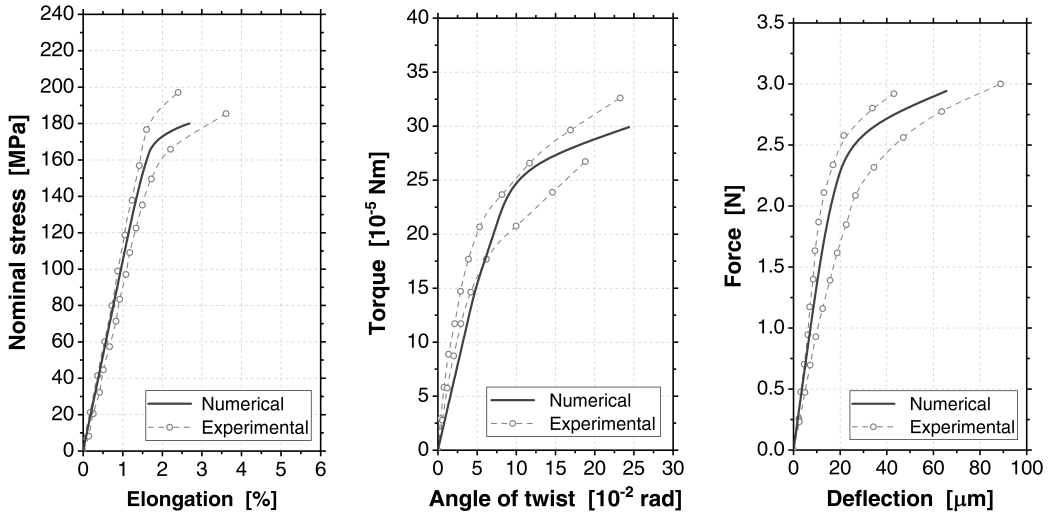

(a) (b) (c)

Fig. 5. Mechanical response of a single osteon in the different loading scenarios investigated: (a) T-test, (b) Θ-test, (c) B-test. In each panel, the load-deformation curve obtained with present model (solid black line) is shown in comparison with two exemplary curves obtained in the corresponding benchmark experiments (dashed gray lines) whose results are available in [31, 62, 63].

- fracture pattern, defined as the set of all elements which experienced interlaminar or intralaminar failure at failure state.

Panels in Fig. 5 report the numerically-experienced load-deformation curves (continuous black lines) obtained in the T-test (Fig. 5(a)), Θ-test (Fig. 5(b)) and B-test (Fig. 5(c)) compared to two exemplary curves (dashed gray lines) corresponding to experimental outcomes available in the previous-cited works. Moreover, Table 5 reports the values of three mechanical parameters characteristic for each loading condition computed with present model, in comparison with the corresponding ones obtained in the benchmark experiments. Obtained numerical results prove that the proposed multiscale constitutive framework is able to accurately describe the mechanical response of single osteons up to failure in different loading scenarios.

The osteon mechanical behaviour predicted by present numerical model is generally characterized by a very rapid propagation of damage. This aspect is suggested by the curves depicted in Fig. 5, which, for each addressed loading condition, approximate to a straight line just shortly before the point of global failure, thus exhibiting a narrow range of load values in the post-elastic regime. Such an evidence is fully in agreement with the experimental findings especially when the T- and B-tests are concerned, as discussed in [31, 63, 66] and as can be seen from the comparison between numerical and experimental curves in Fig. 5. On the other hand, in the case of torsional loading, the

Table 5
Values of the osteon moduli of elasticity, ultimate load and ultimate deformation parameter in T-, Θ- and B-test computed with present model and compared to the experimental values obtained in the benchmark experiments and available in [31, 62, 63]. Experimental values are given in terms of mean value and standard deviation.

Test	**Evaluated parameters**	**Experimental values**	**Present model**
T-test	Tensile modulus of elasticity	(11.68 ± 6.98) GPa	10.47 GPa
	Ultimate tensile strength	(193.48 ± 31.97) MPa	200 MPa
	Elongation at breaking point	(2.15 ± 0.55) %	1.95%
Θ-test	Shear modulus of elasticity	(17.17 ± 3.35) GPa	7.19 GPa
	Ultimate torque	$(31.04 \pm 2.77)\times10^{-5}$ N m	29.91×10^{-5} N m
	Ultimate angular deflection	$(18.09 \pm 4.19)\times10^{-2}$ rad	24.37×10^{-2} rad
B-test	Bending modulus of elasticity	(2.69 ± 0.93) GPa	2.67 GPa
	Ultimate bending load	(2.61 ± 0.38) N	2.70 N
	Ultimate bending deflection	(66.01 ± 17.65) µm	62.26 µm

osteon mechanical behaviour experienced in the tests performed by Ascenzi and coworkers is linear elastic only for low values of the applied load. The deviation from linearity occurs very early with respect to the failure point, suggesting that torsional loading conditions, contrary to the tensile or bending ones, are more prone to induce plastic deformations of bone tissue at lamellar level. Since present model disregards any plastic behaviour of materials, the numerically-predicted deviation from linearity results slightly delayed with respect to the experimental values, and the post-elastic regime is numerically described by a smaller portion of the curve than the experimentally-obtained one.

The stiffness in the elastic regime for T- and B-tests, characterized by the slope of the initial linear branch of the associated loading curve, lies within the range of values predicted by the benchmark experiments (see Table 5). Present model predicts a lower stiffness compared to the experiments only in the case of the Θ-test. Such a discrepancy might be caused by a numerical underestimation of the $\mathbb{C}_{lam,(0)}$ components related to the shear stiffness. However, Ascenzi et al. in [63] highlighted that the modulus of torsional elasticity recorded in the experiments might result overestimated due to some spurious effects that induce an artificial increase of the stiffness, like the end effect of the jaws, the particular aspect ratio (length over diameter) of the specimen tested and the occurrence of axial and/or bending displacement components which are

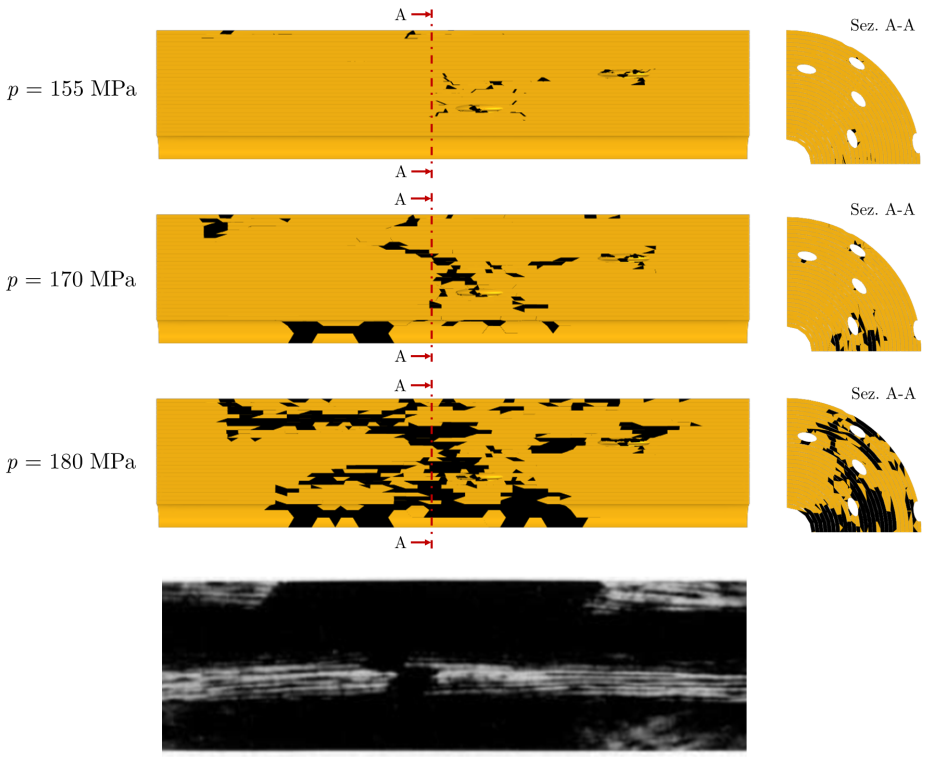

Fig. 6. Onset and evolution of damage pattern for a single osteon loaded in tension (T-test). The value of force per unit area at which the damage pattern is attained is also shown.

constrained by the end conditions. In fact, the predicted modulus of torsional stiffness predicted by present model is instead in accordance with the values found by other authors ([68–70]).

The breaking point, i.e. the point at which global failure of the osteon is experienced, is equally accurately predicted by the numerical model in terms of both ultimate load and corresponding ultimate deformation parameter values. Previous considerations are confirmed by comparing values obtained from present numerical model to the experimental ones available from the benchmark experiments, summarized in Table 5.

Figs. 6, 7 and 8 depict the damage patterns attained at three different increasing values of the applied load predicted by present numerical model when T-, Θ and B-test are addressed, respectively. The fracture pattern experienced in the corresponding benchmark mechanical tests performed by Ascenzi and coworkers is also shown.

The evolution of damage patterns illustrated in Figs. 6, 7 and 8 highlights some aspects of microdamage propagation in single osteons which are in common between the different loading conditions investigated. As expected, the onset of

damage process, corresponding to the point at which a deviation from linearity is noticed in the curves in Fig. 5, occurs particularly in the neighbourhood of lacunae, which acts as stress intensifiers. This evidence emphasizes the fundamental role of the lacunar voids, which therefore cannot be neglected in the numerical modelling of a single osteon. The type of stress which mainly triggers the damage process is obviously dependent on the particular loading condition. Moreover, as highlighted by the pattern of damaged elements in the first row of Figs 6, 7 and 8, both the intralaminar and interlaminar failure criteria equally contribute to microcrack opening and propagation, since failed regions at the beginning of damage propagation involve areas both within the lamellae and between them.

At the failure state, the damage pattern within the osteonal structure predicted in each loading scenario (illustrated in the last row of Figs. 6, 7, 8), resembles the one noticed in the mechanical experiments. In particular, in the case of T-test, as the applied loading increases, failed elements gradually tends to concentrate in the central zone of the osteon, which corresponds to the region having an higher local density of lacunae. As a consequence, the predicted main fracture surface, which may be identified with an uninterrupted sequence of failed elements, approximately passes through the central zone of the osteon. These findings are perfectly in-line with the experimental fracture patterns observed by Ascenzi and Bonucci in [62], as can be also seen in Fig. 6. The numerically-predicted damage pattern at failure state in the case of a torsional loading condition appears as the most irregular one, with several multiple cracks whose initial obliquity with respect to the osteon long axis is generally around 45° (see Fig. 7), approximately following a direction almost

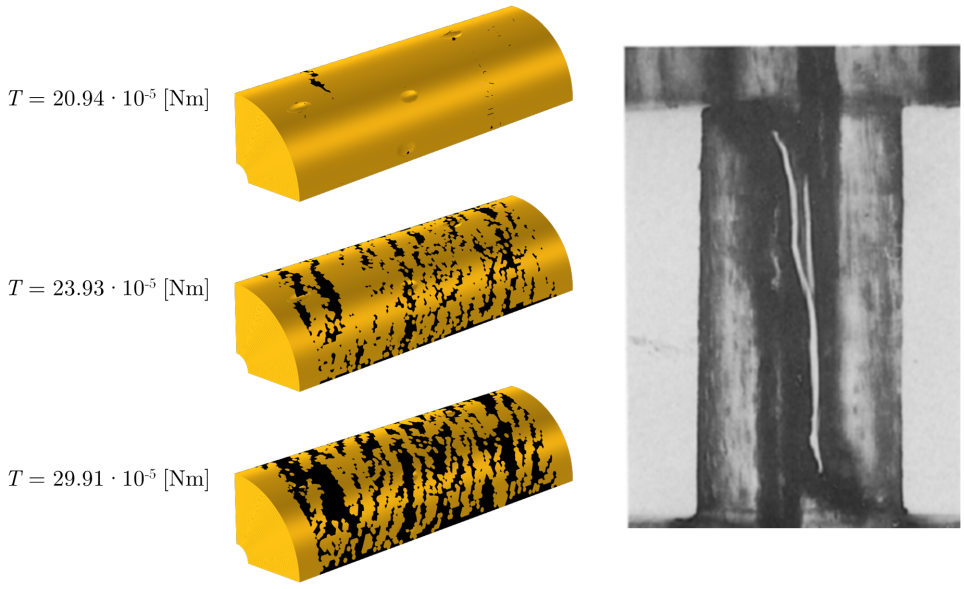

Fig. 7. Onset and evolution of damage pattern for a single osteon loaded in torsion (Θ-test). The value of torque at which the damage pattern is attained is also shown.

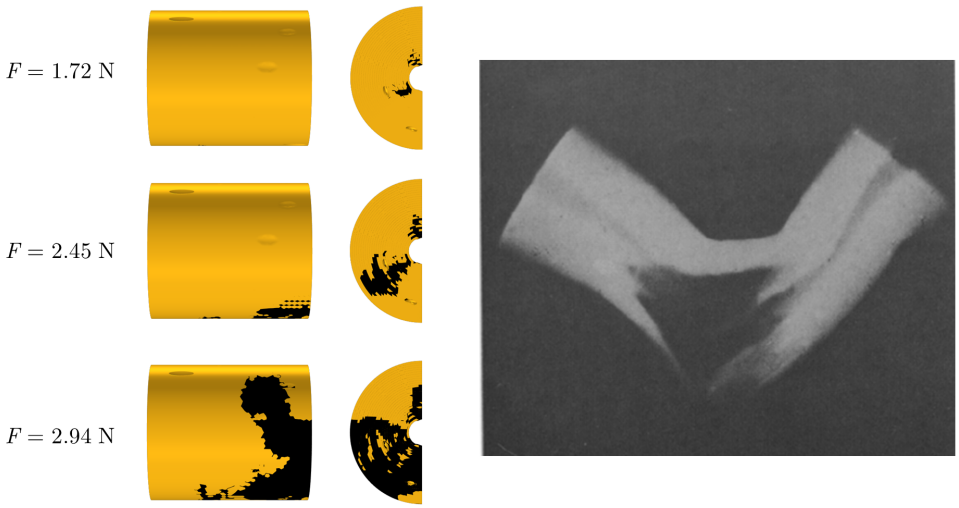

Fig. 8. Onset and evolution of damage pattern for a single osteon loaded in bending (B-test). The value of bending load at which the damage pattern is attained is also shown.

parallel to the orientation of the majority of MCFs. Such an evidence is again in line with the experimental findings since, as stated by Ascenzi et al. in [63], for many tested osteon samples "cracks affected osteons at a variety of level". Finally, by addressing the B-test, numerically-experienced failure zone is located on the tension side of the central part of the osteon, in agreement with the experimental evidence reported in [31] (see Fig. 8). Specifically, the failure mechanism under a bending load results as a quick spread of damage originating in the area around the Haversian canal and gradually propagating towards the compressive side of the osteon.

3.3 Sensitivity analysis with respect to the tissue degree of mineralization

Several evidence proved that biological factors such as ageing or the occurrence of disease affect the structure and composition of bone tissue at each length scale, mainly causing a decrease in the degree of mineralization [16,71]. Therefore, aiming to assess the predictability of present multiscale model in case of biophysical alterations of bone tissue, a parametric study with respect to the degree of mineralization Φ has been carried out to assess the sensitivity of the model. In particular, the MCFs equivalent properties have been obtained by employing values of $\Phi \in \{0.20, 0.30, 0.40\}$, where the highest value is considered as representative of a perfectly healthy tissue while the lowest one of a low calcified tissue [9,16]. In this concern, owing to the high number of geometrical and constitutive variables involved, only the along-the-fibril-axis crystal edge length ℓ_{HA} has been varied. Indeed, both the crystal thickness b_{HA}

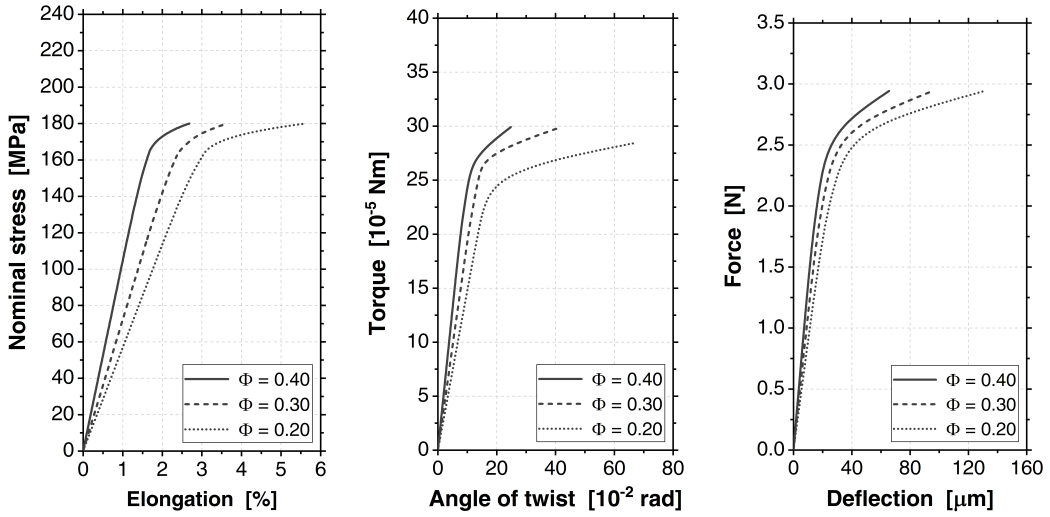

(a) (b) (c)

Fig. 9. Effect of HA volume fraction at the nanoscale on the mechanical behaviour of a single osteon in the different loading scenarios investigated: (a) T-test, (b) Θ-test, (c) B-test.

and depth d_{HA}, as well as the lateral spacings between adjacent HA platelets Δb and Δd show a very limited range of variability, as well-documented in the literature [9, 36, 52].

Panels in Fig. 9 report the curves representative of the mechanical behaviour of a single osteon loaded in tension (Fig. 9(a)), in torsion (Fig. 9(b)) and bending (Fig. 9(c)) for values of HA volume fraction equal to herein considered. It can be clearly seen that such a nanostructural parameter deeply affects the mechanical response of cortical bone at the microscale. In particular, moving from $\Phi = 0.40$ to $\Phi = 0.20$, the stiffness reduces by 45.7%, 43.6% and 35.2% for the T-, Θ- and B-tests, respectively. On the other hand, that the point of deviation from linearity is almost independent from the HA volume fraction Φ, especially for the tensile and bending loading conditions. Such an evidence is probably a consequence of the herein-assumed hypothesis of independence of the strength parameters from Φ, situation which is well-documented in the literature (see e.g. [72]). Similarly, the post-elastic regime is described by a range of load values approximately independent from Φ. In the case of Θ-test, a decrease in the degree of mineralization reflects mainly in a decrease of the torsional load value at which deviation from linearity occurs, and not in a widening or narrowing of the post-elastic range of load values. On the other hand, the deformation experienced up to the point of global failure result higher for lower values of Φ. Previous considerations are in accordance with the outcomes of tensile tests conducted on single osteons by Ascenzi et al., who tested several osteon samples having both a high and low degree of mineralization [66]. Unfortunately, the influence of bone mineral content on the

experimental-based mechanical behaviour of single osteons for torsional and bending loading conditions was not analyzed by the authors, and therefore a direct comparison could not have been made. Nevertheless, since numerical results obtained for different values of mineral content closely match to the experimental ones for the T-test, and due to the similarity between the experimental and numerical curves for a fully calcified tissue ($\Phi = 0.40$), it can be assumed that present multiscale model characterizing a single osteon as a perfectly brittle material with a stress-based damage description furnish accurate results for all values of Φ in several loading conditions. Obtained fracture patterns recorded for the values of *Phi* herein investigated are similar to the ones illustrated through the text, and have not herein reported for the sake of brevity.

4 Concluding remarks

In this paper, the mechanical response of a single osteon (i.e. of cortical bone tissue at the sub-macroscale level) has been numerically investigated by adopting a multiscale constitutive framework, implemented in home-made FE-based codes. In detail, the geometry of a typical osteon has been reconstructed by considering the osteon as a multi-layered hollow cylinder made up of several coaxial cylindrical lamellae. All the geometrical dimensions have been established based on average values found in the literature. Homogeneous anisotropic constitutive properties of lamellar tissue have been obtained via a bottom-up multistep homogenization approach starting from the nanoscale, and the effect of the interlamellar areas, modelled as thin elastic interfaces between two subsequent lamellae, has been accounted for. A progressive damage approach has been implemented to model the osteon as a perfectly-brittle material.

The proposed computational approach has been validated by simulating in a FE framework three different loading conditions of which experimental results were available. Presented results highlighted that the present refined modelling strategy is able to accurately predict and describe the mechanical behaviour of typical single osteons up to complete failure in many loading conditions. Moreover, a stress-driven damage evolution revealed effective in describing the mechanical response of the osteon when different values of the bone degree of mineralization are considered. Specifically, as the mineralization degree decreases, a rather marked decrease in the stiffness, a more extended post-elastic phase in terms of deformation and an invariance of the point of damage onset have been predicted. As a consequence, proposed model is able to account for the influence of nanostructural features and parameters on the osteon global mechanical response at the sub-macroscale.

Accordingly, proposed numerical procedure provides an insight on the microscale failure mechanisms of bone structures which can be useful for defining refined bottom-up constitutive descriptions of cortical bone tissue at the organ level. Moreover, present model opens towards the prediction of bone mechanical behaviour when disease- or ageing-induced structural and/or morphological alterations in any of the bone micro- or nano-structural features (e.g., variations in the collagen fibres orientations, thinning of lamellae, increasing in the lacunae volume fraction, alteration in the morphology and shape of HA platelets) occur.

Future work will be devoted to perform parametric studies on the previously-mentioned micro- and nano-structural parameters, as well as to overcome the limitations of present study. More irregular geometries and possible residual stress and prestress will be considered. Plasticity effects will be taken into account to describe more accurately the osteon mechanical response, especially when torsional stress is present. Furthermore, the non-linear mechanics of collagen fibrils at the nanoscale, which is governed by both entropic and energetic mechanisms, will be included in order to characterize more effectively the mechanical response of mineralized collagen fibrils, especially in the case of very low values of bone degree of mineralization.

A Matrix form of stress and strain transformation tensors

Let $\{Opqr\}$ and $\{Op'q'r'\}$ be two different orthogonal cartesian coordinate systems. The positions of axes p', q', r' with respect to axes p, q, r can be specified by means of three angles Θ_p, Θ_q, Θ_r representing the angles of consecutive rotations of primed system $\{Op'q'r'\}$ about the p, q, r axes, respectively, taken positive in the counterclockwise direction. In present model, for the j-th sublayer constituting a given lamella, it results $\Theta_p = \chi_j$, $\Theta_q = 0$ and $\Theta_r = \psi_j$, respectively. Moreover, let symbols $c_h = \cos\Theta_h$, $s_h = \sin\Theta_h$ ($h \in \{p, q, r\}$) be introduced for the sake of compactness. Then, the matrix form of tensors $\mathbb{T}_j$ and $\mathbb{D}_j$ employed in Eq. (7) is [44]:

$$\mathbb{T}_j = \mathbb{T}_j^p \, \mathbb{T}_j^q \, \mathbb{T}_j^r \tag{A.1}$$

$$\mathbb{D}_j = \mathbb{D}_j^p \, \mathbb{D}_j^q \, \mathbb{D}_j^r \tag{A.2}$$

where:

$$\mathbb{T}_j^p = \begin{bmatrix} 1 & 0 & 0 & 0 & 0 & 0 \\ 0 & c_p^2 & s_p^2 & 2c_p s_p & 0 & 0 \\ 0 & s_p^2 & c_p^2 & -2c_p s_p & 0 & 0 \\ 0 & -c_p s_p & c_p s_p & c_p^2 - s_p^2 & 0 & 0 \\ 0 & 0 & 0 & 0 & c_p & -s_p \\ 0 & 0 & 0 & 0 & s_p & c_p \end{bmatrix} \tag{A.3}$$

$$\mathbb{T}_j^q = \begin{bmatrix} c_q^2 & 0 & s_q^2 & 0 & 2c_q s_q & 0 \\ 0 & 1 & 0 & 0 & 0 & 0 \\ s_q^2 & 0 & c_q^2 & 0 & -2c_q s_q & 0 \\ 0 & 0 & 0 & c_q & 0 & -s_q \\ -c_q s_q & 0 & c_q s_q & 0 & c_q^2 - s_q^2 & 0 \\ 0 & 0 & 0 & s_q & 0 & c_q \end{bmatrix} \tag{A.4}$$

$$\mathbb{T}_j^r = \begin{bmatrix} c_r^2 & s_r^2 & 0 & 0 & 0 & 2c_r s_r \\ s_r^2 & c_r^2 & 0 & 0 & 0 & -2c_r s_r \\ 0 & 0 & 1 & 0 & 0 & 0 \\ 0 & 0 & 0 & c_r & -s_r & 0 \\ 0 & 0 & 0 & s_r & c_r & 0 \\ -c_r s_r & c_r s_r & 0 & 0 & 0 & c_r^2 - s_r^2 \end{bmatrix} \tag{A.5}$$

$$\mathbb{D}_j^p = \begin{bmatrix} 1 & 0 & 0 & 0 & 0 & 0 \\ 0 & c_p^2 & s_p^2 & c_p s_p & 0 & 0 \\ 0 & s_p^2 & c_p^2 & -c_p s_p & 0 & 0 \\ 0 & -2c_p s_p & 2c_p s_p & c_p^2 - s_p^2 & 0 & 0 \\ 0 & 0 & 0 & 0 & c_p & -s_p \\ 0 & 0 & 0 & 0 & s_p & c_p \end{bmatrix} \tag{A.6}$$

$$\mathbb{D}_j^q = \begin{bmatrix} c_q^2 & 0 & s_q^2 & 0 & c_q s_q & 0 \\ 0 & 1 & 0 & 0 & 0 & 0 \\ s_q^2 & 0 & c_q^2 & 0 & -c_q s_q & 0 \\ 0 & 0 & 0 & c_q & 0 & -s_q \\ -2c_q s_q & 0 & 2c_q s_q & 0 & c_q^2 - s_q^2 & 0 \\ 0 & 0 & 0 & s_q & 0 & c_q \end{bmatrix} \tag{A.7}$$

$$\mathbb{D}_j^r = \begin{bmatrix} c_r^2 & s_r^2 & 0 & 0 & 0 & c_r s_r \\ s_r^2 & c_r^2 & 0 & 0 & 0 & -c_r s_r \\ 0 & 0 & 1 & 0 & 0 & 0 \\ 0 & 0 & 0 & c_r & -s_r & 0 \\ 0 & 0 & 0 & s_r & c_r & 0 \\ -2c_r s_r & 2c_r s_r & 0 & 0 & 0 & c_r^2 - s_r^2 \end{bmatrix} \tag{A.8}$$

References

[1] I. Fleps, A. Fung, P. Guy, S. J. Ferguson, B. Helgason, P. A. Cripton, Subject-specific ex vivo simulations for hip fracture risk assessment in sideways falls, Bone 125 (2019) 36–45.

[2] P. Carpintero, J. R. Caeiro, R. Carpintero, A. Morales, S. Silva, M. Mesa, Complications of hip fractures: a review, World journal of orthopedics 5 (4) (2014) 402.

[3] O. Guzon-Illescas, E. P. Fernandez, N. C. Villarias, F. J. Q. Donate, M. Peña, C. Alonso-Blas, A. García-Vadillo, R. Mazzucchelli, Mortality after osteoporotic hip fracture: incidence, trends, and associated factors, Journal of orthopaedic surgery and research 14 (1) (2019) 1–9.

[4] A. R. Kemmak, A. Rezapour, R. Jahangiri, S. Nikjoo, H. Farabi, S. Soleimanpour, Economic burden of osteoporosis in the world: A systematic review, Medical Journal of the Islamic Republic of Iran 34 (2020) 154.

[5] S. A. Williams, S. G. Daigle, R. Weiss, Y. Wang, T. Arora, J. R. Curtis, Economic burden of osteoporosis-related fractures in the us medicare population, Annals of Pharmacotherapy (2020) 1060028020970518.

[6] F. Eggermont, G. Van Der Wal, P. Westhoff, A. Laar, M. De Jong, T. Rozema, H. M. Kroon, O. Ayu, L. Derikx, S. Dijkstra, et al., Patient-specific finite

element computer models improve fracture risk assessments in cancer patients with femoral bone metastases compared to clinical guidelines, Bone 130 (2020) 115101.

[7] K. L. Stone, D. G. Seeley, L.-Y. Lui, J. A. Cauley, K. Ensrud, W. S. Browner, M. C. Nevitt, S. R. Cummings, BMD at multiple sites and risk of fracture of multiple types: long-term results from the study of osteoporotic fractures, Journal of Bone and Mineral Research 18 (11) (2003) 1947–1954.

[8] M. L. Bouxsein, Determinants of skeletal fragility, Best practice & research Clinical rheumatology 19 (6) (2005) 897–911.

[9] J.-Y. Rho, L. Kuhn-Spearing, P. Zioupos, Mechanical properties and the hierarchical structure of bone, Medical engineering & physics 20 (2) (1998) 92–102.

[10] N. Reznikov, R. Shahar, S. Weiner, Bone hierarchical structure in three dimensions, Acta biomaterialia 10 (9) (2014) 3815–3826.

[11] S. Weiner, W. Traub, Bone structure: from ångstroms to microns, The FASEB journal 6 (3) (1992) 879–885.

[12] A. Ural, D. Vashishth, Hierarchical perspective of bone toughness–from molecules to fracture, International Materials Reviews 59 (5) (2014) 245–263.

[13] S. Weiner, W. Traub, H. D. Wagner, Lamellar bone: structure–function relations, Journal of structural biology 126 (3) (1999) 241–255.

[14] M.-M. Giraud-Guille, Twisted plywood architecture of collagen fibrils in human compact bone osteons, Calcified tissue international 42 (3) (1988) 167–180.

[15] W. Landis, M. Song, A. Leith, L. McEwen, B. McEwen, Mineral and organic matrix interaction in normally calcifying tendon visualized in three dimensions by high-voltage electron microscopic tomography and graphic image reconstruction, Journal of structural biology 110 (1) (1993) 39–54.

[16] S. C. Cowin, et al., Bone mechanics handbook, CRC press, 2001.

[17] M. J. Olszta, X. Cheng, S. S. Jee, R. Kumar, Y.-Y. Kim, M. J. Kaufman, E. P. Douglas, L. B. Gower, Bone structure and formation: A new perspective, Materials Science and Engineering: R: Reports 58 (3-5) (2007) 77–116.

[18] E. Hamed, I. Jasiuk, Multiscale damage and strength of lamellar bone modeled by cohesive finite elements, journal of the mechanical behavior of biomedical materials 28 (2013) 94–110.

[19] F. Barthelat, R. Rabiei, Toughness amplification in natural composites, Journal of the Mechanics and Physics of Solids 59 (4) (2011) 829–840.

[20] P. Zioupos, J. Currey, Changes in the stiffness, strength, and toughness of human cortical bone with age, Bone 22 (1) (1998) 57–66.

[21] G. P. Parsamian, T. L. Norman, Diffuse damage accumulation in the fracture process zone of human cortical bone specimens and its influence on fracture toughness, Journal of Materials Science: Materials in Medicine 12 (9) (2001) 779–783.

[22] D. Vashishth, Hierarchy of bone microdamage at multiple length scales, International journal of fatigue 29 (6) (2007) 1024–1033.

[23] F. A. Sabet, A. Raeisi Najafi, E. Hamed, I. Jasiuk, Modelling of bone fracture and strength at different length scales: a review, Interface focus 6 (1) (2016) 20150055.

[24] H. A. Hogan, Micromechanics modeling of haversian cortical bone properties, Journal of biomechanics 25 (5) (1992) 549–556.

[25] J. Crolet, B. Aoubiza, A. Meunier, Compact bone: numerical simulation of mechanical characteristics, Journal of biomechanics 26 (6) (1993) 677–687.

[26] P. J. Prendergast, R. Huiskes, Microdamage and osteocyte-lacuna strain in bone: a microstructural finite element analysis, Journal of biomechanical engineering 118 (2) (1996) 240–246.

[27] X. Guo, L. Liang, S. Goldstein, Micromechanics of osteonal cortical bone fracture.

[28] A. R. Najafi, A. R. Arshi, M. Eslami, S. Fariborz, M. H. Moeinzadeh, Micromechanics fracture in osteonal cortical bone: A study of the interactions between microcrack propagation, microstructure and the material properties, Journal of Biomechanics 40 (12) (2007) 2788–2795.

[29] E. Giner, C. Arango, A. Vercher, F. J. Fuenmayor, Numerical modelling of the mechanical behaviour of an osteon with microcracks, Journal of the mechanical behavior of biomedical materials 37 (2014) 109–124.

[30] A. Ascenzi, E. Bonucci, A. Simkin, An approach to the mechanical properties of single osteonic lamellae, Journal of biomechanics 6 (3) (1973) 227–235.

[31] A. Ascenzi, P. Baschieri, A. Benvenuti, The bending properties of single osteons, Journal of biomechanics 23 (8) (1990) 763–771.

[32] J. A. Petruska, A. J. Hodge, A subunit model for the tropocollagen macromolecule, Proceedings of the National Academy of Sciences of the United States of America 51 (5) (1964) 871.

[33] W. Landis, The strength of a calcified tissue depends in part on the molecular structure and organization of its constituent mineral crystals in their organic matrix, Bone 16 (5) (1995) 533–544.

[34] R. A. Robinson, An electron-microscopic study of the crystalline inorganic component of bone and its relationship to the organic matrix, JBJS 34 (2) (1952) 389–476.

[35] I. Jäger, P. Fratzl, Mineralized collagen fibrils: a mechanical model with a staggered arrangement of mineral particles, Biophysical journal 79 (4) (2000) 1737–1746.

[36] A. Vercher, E. Giner, C. Arango, J. E. Tarancón, F. J. Fuenmayor, Homogenized stiffness matrices for mineralized collagen fibrils and lamellar bone using unit cell finite element models, Biomechanics and modeling in mechanobiology 13 (2) (2014) 437–449.

[37] S. Nikolov, D. Raabe, Hierarchical modeling of the elastic properties of bone at submicron scales: the role of extrafibrillar mineralization, Biophysical journal 94 (11) (2008) 4220–4232.

[38] F. Maceri, M. Marino, G. Vairo, A unified multiscale mechanical model for soft collagenous tissues with regular fiber arrangement, Journal of biomechanics 43 (2) (2010) 355–363.

[39] S. Torquato, Effective stiffness tensor of composite media: Ii. applications to isotropic dispersions, Journal of the Mechanics and Physics of Solids 46 (8) (1998) 1411–1440.

[40] R. C. McPhedran, G. W. Milton, Bounds and exact theories for the transport properties of inhomogeneous media, Applied Physics A 26 (4) (1981) 207–220.

[41] J. Eischen, S. Torquato, Determining elastic behavior of composites by the boundary element method, Journal of applied physics 74 (1) (1993) 159–170.

[42] R. Hill, Theory of mechanical properties of fibre-strengthened materials: I. elastic behaviour, Journal of the Mechanics and Physics of Solids 12 (4) (1964) 199–212.

[43] U. Akiva, H. D. Wagner, S. Weiner, Modelling the three-dimensional elastic constants of parallel-fibred and lamellar bone, Journal of Materials Science 33 (6) (1998) 1497–1509.

[44] L. P. Kollar, G. S. Springer, Mechanics of composite structures, Cambridge university press, 2003.

[45] O. L. Katsamenis, H. M. Chong, O. G. Andriotis, P. J. Thurner, Load-bearing in cortical bone microstructure: Selective stiffening and heterogeneous strain distribution at the lamellar level, Journal of the mechanical behavior of biomedical materials 17 (2013) 152–165.

[46] F. Barthelat, Z. Yin, M. J. Buehler, Structure and mechanics of interfaces in biological materials, Nature Reviews Materials 1 (4) (2016) 1–16.

[47] G. Marotti, V. Cane, S. Palazzini, C. Palumbo, Structure-function relationships in the osteocyte.

[48] H. Sissons, P. O'Connor, Quantitative histology of osteocyte lacunae in normal human cortical bone, Calcified tissue research 22 (1) (1976) 530–533.

[49] J. C. Brewer, P. A. Lagace, Quadratic stress criterion for initiation of delamination, Journal of composite materials 22 (12) (1988) 1141–1155.

[50] T. Hassenkam, G. E. Fantner, J. A. Cutroni, J. C. Weaver, D. E. Morse, P. K. Hansma, High-resolution afm imaging of intact and fractured trabecular bone, Bone 35 (1) (2004) 4–10.

[51] E. Hamed, Y. Lee, I. Jasiuk, Multiscale modeling of elastic properties of cortical bone, Acta mechanica 213 (1) (2010) 131–154.

[52] H. A. Lowenstam, S. Weiner, et al., On biomineralization, Oxford University Press on Demand, 1989.

[53] S. Cusack, A. Miller, Determination of the elastic constants of collagen by brillouin light scattering, Journal of molecular biology 135 (1) (1979) 39–51.

[54] M. J. Buehler, Nanomechanics of collagen fibrils under varying cross-link densities: atomistic and continuum studies, Journal of the mechanical behavior of biomedical materials 1 (1) (2008) 59–67.

[55] J. L. Katz, Hard tissue as a composite materiali. bounds on the elastic behavior, Journal of biomechanics 4 (5) (1971) 455–473.

[56] H. Yao, L. Ouyang, W.-Y. Ching, Ab initio calculation of elastic constants of ceramic crystals, Journal of the American Ceramic Society 90 (10) (2007) 3194–3204.

[57] R. Pidaparti, A. Chandran, Y. Takano, C. Turner, Bone mineral lies mainly outside collagen fibrils: predictions of a composite model for osternal bone, Journal of biomechanics 29 (7) (1996) 909–916.

[58] H. D. Wagner, S. Weiner, On the relationship between the microstructure of bone and its mechanical stiffness, Journal of Biomechanics 25 (11) (1992) 1311–1320.

[59] M. A. Rubin, I. Jasiuk, J. Taylor, J. Rubin, T. Ganey, R. P. Apkarian, Tem analysis of the nanostructure of normal and osteoporotic human trabecular bone, Bone 33 (3) (2003) 270–282.

[60] P. Suquet, Homogenization techniques for composite media, Springer, 1987.

[61] M. Hori, S. Nemat-Nasser, On two micromechanics theories for determining micro–macro relations in heterogeneous solids, Mechanics of materials 31 (10) (1999) 667–682.

[62] A. Ascenzi, E. Bonucci, The tensile properties of single osteons, The Anatomical Record 158 (4) (1967) 375–386.

[63] A. Ascenzi, P. Baschieri, A. Benvenuti, The torsional properties of single selected osteons, Journal of Biomechanics 27 (7) (1994) 875–884.

[64] X. N. Dong, X. Zhang, X. E. Guo, Interfacial strength of cement lines in human cortical bone, Molecular & Cellular Biomechanics 2 (2) (2005) 63.

[65] R. F. Bigley, L. V. Griffin, L. Christensen, R. Vandenbosch, Osteon interfacial strength and histomorphometry of equine cortical bone, Journal of biomechanics 39 (9) (2006) 1629–1640.

[66] A. Ascenzi, A. Benvenuti, E. Bonucci, The tensile properties of single osteonic lamellae: technical problems and preliminary results, Journal of biomechanics 15 (1) (1982) 29–37.

[67] P. Gaziano, C. Lorenzi, D. Bianchi, E. Monaldo, A. Dolci, G. Vairo, Mechanical performance of anatomic-functional-geometry dental treatments: A computational study, Medical Engineering & Physics 86 (2020) 96–108.

[68] W. Bonfield, C. Li, Anisotropy of nonelastic flow in bone, Journal of Applied Physics 38 (6) (1967) 2450–2455.

[69] H. S. Yoon, J. L. Katz, Ultrasonic wave propagation in human cortical boneii. measurements of elastic properties and microhardness, Journal of biomechanics 9 (7) (1976) 459–464.

[70] P. Frasca, R. Harper, J. L. Katz, Strain and frequency dependence of shear storage modulus for human single osteons and cortical bone microsamplessize and hydration effects, Journal of biomechanics 14 (10) (1981) 679–690.

[71] E. A. Zimmermann, E. Schaible, H. Bale, H. D. Barth, S. Y. Tang, P. Reichert, B. Busse, T. Alliston, J. W. Ager, R. O. Ritchie, Age-related changes in the plasticity and toughness of human cortical bone at multiple length scales, Proceedings of the National Academy of Sciences 108 (35) (2011) 14416–14421.

[72] A. Ascenzi, E. Bonucci, The ultimate tensile strength of single osteons, Cells Tissues Organs 58 (1-2) (1964) 160–183.